

Rotating stellar populations in the Fornax dSph galaxy

Andrés del Pino^{1*}, Antonio Aparicio^{2,3}, Sebastian L. Hidalgo^{2,3} and Ewa L. Lokas¹

¹*Nicolaus Copernicus Astronomical Center, Polish Academy of Sciences, Bartycka 18, 00-716 Warsaw, Poland*

²*Instituto de Astrofísica de Canarias, Calle Vía Láctea s/n, E-38200 La Laguna, Tenerife, Spain*

³*Departamento de Astrofísica, Universidad de La Laguna, Avda. Astrofísico Fco. Sánchez s/n, E-38206 La Laguna, Tenerife, Spain*

21 November 2016

ABSTRACT

We present a novel analysis of the internal kinematics of the Fornax dwarf spheroidal galaxy. Our results are based on the largest sample of spectroscopic data for Fornax stars presently available (> 2500 stars), for which we have chemical and kinematic information. We introduce new software, BEACON, designed to detect chemo-kinematic patterns among stars of different stellar populations using their metallicity and velocity along the line of sight. Applying BEACON to Fornax we have detected non-negligible rotation signals around main optical axes of the galaxy, characteristic for a triaxial system partially supported by rotation. The dominant rotation pattern is relatively strong ($\sim 12 \text{ km s}^{-1}$), but the galaxy also shows additional weaker albeit complex rotation patterns. Using the information available from the star formation history of Fornax we have also derived the average age of the different chemo-kinematic components found by BEACON, which has allowed us to obtain its kinematic history. Our results point to a possible major merger suffered by Fornax at redshift $z \sim 1$, in agreement with previous works.

Key words: galaxies: evolution – galaxies: Local Group – galaxies: dwarf – galaxies: kinematics and dynamics – galaxies: interactions – galaxies: individual: Fornax

1 INTRODUCTION

Dwarf galaxies comprise the most common type of galaxies in the Universe, however even in the Local Group the details of the internal kinematics of many of them remain unknown. This is specially true for the most recently discovered ultra faint dwarfs, but also for many of the well known classical dwarf spheroidal (dSph) galaxies. There are several reasons for this; some of them more technical or observational, others more conceptual.

The first of the observational issues is related to their relatively large distances, up to $(m - M)_0 \sim 24$ for many of the M31 satellites (McConnachie 2012). Observations of these objects thus require the use of large telescopes and even then obtaining e.g. the proper motions of their stars remains extremely difficult. The second main technical problem is the fact that dSph galaxies retain very little gas. Consequently, the spectra of a large number of their stars must be obtained in order to reliably study their kinematics. This has posed a technological challenge and only in the most nearby galaxies a sufficient number of stars have been measured to provide solid results.

Some of the classical dSphs have been repeatedly studied during the last decade. In most of them, no obvious signs

of rotation were found (Wilkinson et al. 2004; Muñoz et al. 2005; Koch et al. 2007a,b; Walker et al. 2009a; Wheeler et al. 2015). In the case of the Milky Way (MW) satellites, the evidence for gradients in the line-of-sight velocity (v_{LOS}) along the optical axes is most convincing for Fornax, Sculptor and Sextans dSphs (Battaglia et al. 2008a, 2011; Amorisco & Evans 2012). However, the absence of reliably measured proper motions for some of these galaxies makes it unclear whether these gradients are the intrinsic rotation signal or rather produced by geometrical effects (Walker et al. 2008; Strigari et al. 2010). Therefore, dSph galaxies have been generally considered to be pressure-supported systems with little or no rotation.

From the cosmological point of view, dSphs are likely to be examples of the evolved state of late-type dwarfs, transformed into spheroids as a result of tidal stirring, ram pressure and other environmental effects (Mayer 2010, and references therein). If this scenario is correct, some residual rotation signal should be present in these galaxies. Could these rotation signals have escaped detection due to the large velocity dispersions of these systems? In the case they do not rotate at all, how did they acquire their spheroidal shapes and are not simply spherical as globular clusters? These questions encouraged us to develop BEACON, a code designed specifically for finding chemo-kinematic patterns in

* E-mail: adpm@camk.edu.pl

resolved stellar systems. In this paper, we test the capabilities of BEACON and apply it to the Fornax dSph galaxy.

With about ~ 2500 likely member stars observed, Fornax represents the state-of-the-art system in terms of spectroscopic observations in dSph galaxies. Fornax is, after the Sagittarius dSph, the largest and most luminous of the dSph MW companions, with a core radius of $16.6' \sim 550$ pc. It is located at a distance of 136 ± 5 kpc (Mackey & Gilmore 2003; Greco et al. 2007, 2009; Tammann, Sandage & Reindl 2008; Poretti et al. 2008), and its principal baryonic component is stellar, with an ambiguous detection of HI (Bouchard, Carignan & Staveley-Smith 2006) possibly associated with the MW. The dynamical mass within the observed half-light radius has been estimated to be $5.6 \times 10^7 M_\odot$ (McConnachie 2012, and references therein), while the total mass (assuming mass follows light) is $1.6 \times 10^8 M_\odot$ (Lokas 2009). The observational properties of the Fornax dwarf are summarized in Table 1.

Fornax is a remarkable object to study. Together with Sagittarius, it is the only dSph among MW companions harbouring a system of globular clusters. Its star formation history (SFH) is long-lasting and complex, showing strong spatial gradients between the centre and the outskirts of the galaxy (de Boer et al. 2012; del Pino et al. 2013). This can be also viewed as a clear spatial segregation between its different stellar populations (del Pino et al. 2015). Moreover, its young stellar populations are not symmetrically distributed in the galaxy, showing stellar clumps and structures not aligned with the optical axes. The most famous ones are the shell-like overdensities located at $17'$ and 1.3° from the centre, although the latter has been recently claimed to be in fact an overdensity of background galaxies (Bate et al. 2015). Its internal dynamics also appears to be rather complex, leading to diverse results and interpretations concerning the past of the galaxy (Walker et al. 2009a; Amorisco & Evans 2012; Hendricks et al. 2014).

All these observational facts have stoked a debate about the possibility that Fornax suffered a merger. Some authors claim that these stellar substructures are the result of a past merger (Coleman et al. 2004; Coleman & Da Costa 2005; Amorisco & Evans 2012; Yozin & Bekki 2012; del Pino et al. 2015). On the other hand, de Boer et al. (2013) claim that these clumps are more likely the result of a quiet infall of gas previously expelled from Fornax during its star formation episodes.

The large amount of data available for Fornax together with its apparently complex past have made of this galaxy a perfect target for testing BEACON. In this paper, we applied the code on the largest ensemble of spectroscopic data for Fornax stars available to date. In Section 2 the data set is presented and we explain the internal calibration between catalogues we performed. Section 3 describes BEACON. In Section 4 we present the results of its application to Fornax. In Section 5, consistency tests and their results are described. Our results are discussed in Section 6. Finally, a summary and the main conclusions of the paper are presented in Section 7.

Table 1. Observational parameters of the Fornax dSph.

Quantity	Value	Reference ^a
RA, α (J2000.0)	2h 39' 53.1''	(3)
Dec, δ (J2000.0)	-34° 30' 16.0''	(3)
Heliocentric velocity (km s ⁻¹)	55.3 ± 0.1	(4)
Ellipticity, e	0.30 ± 0.01	(1)
Position angle (°)	41 ± 6	(1)
Core radius (')	13.8 ± 0.8	(2)
Tidal radius (')	71 ± 4	(2)

^a (1) Irwin & Hatzidimitriou (1995); (2) Mateo (1998); (3) van den Bergh (1999); (4) McConnachie (2012).

2 DATA

There is a large number of spectroscopic measurements for red giant branch (RGB) stars in Fornax. These comprise data collected with a variety of instruments, resolution and scientific aims. Therefore, not all available catalogues provide equally comprehensive information, nor of the same quality. In principle, to get the most complete information about each star (e.g. α -element abundances) it would be desirable to have high resolution spectroscopy with a good signal-to-noise (S/N) ratio. Since this is not the case for a vast majority of the observed stars in Fornax, it is then preferable to have more basic information but for as many stars as possible. For this reason, we have based our study only on the metallicity ([Fe/H]) and line-of-sight velocities (v_{LOS}), which are commonly provided by most of the available spectroscopic catalogues for Fornax. We decided to collect this information from the catalogues with the largest number of observed stars in Fornax (Pont et al. 2004; Battaglia et al. 2006, 2008b; Walker et al. 2009a; Kirby et al. 2010; Letarte et al. 2010).

2.1 The calcium triplet

The infrared Ca II triplet lines (CaT) have been repeatedly measured for more than a 1000 stars in Fornax (Pont et al. 2004; Battaglia et al. 2008b; Kirby et al. 2010; Letarte et al. 2010). In terms of metallicity these works provide rather consistent results (see del Pino et al. 2013, for further information). Notwithstanding, the different metallicity scales used in each study make a direct comparison between catalogues difficult. In order to make all metallicities compatible with each other we have rescaled each catalogue to the metallicity scale of Battaglia et al. (2008b) (B08 hereafter) using the Starkenburg et al. (2010) calibration. This scale was preferred since the age-metallicity relation (AMR) obtained using their data is in good agreement with the one obtained from deep VLT photometry (del Pino et al. 2013).

Letarte et al. (2010), provide v_{LOS} as well as the associated errors for their observed stars in their table A.1. In the case of B08 and Kirby et al. (2010), these quantities were kindly provided by the authors. In order to obtain v_{LOS} for Pont et al. (2004) stars, we cross-matched these with the Walker et al. (2009a) (W09 hereafter) catalogue. Only good matches were saved in the final catalogue, keeping the recalibrated metallicities from (Pont et al. 2004) and

the v_{LOS} from W09. In total, we used 1369 stars from these catalogues.

2.2 The magnesium triplet

The W09 spectra sample the $\sim 5160 \text{ \AA}$ region, which contains the magnesium triplet absorption lines. The metallicities obtained in this work differ significantly from the rest of the catalogues. We believe this is an effect caused by an incomplete sky subtraction in some of their measurements, since their linear model works correctly in their calibration globular clusters. In order to be able to compare the W09 stars with the rest of the sample, we recalculated their metallicities using the [Starkenburg et al. \(2010\)](#) empirical model with their ΣMg composite index ($\langle\Sigma\text{Mg}\rangle$ when several measurements were available). The [Starkenburg et al. \(2010\)](#) model defines the metallicity of a star, $[\text{Fe}/\text{H}]_{\text{cal}}$, as:

$$[\text{Fe}/\text{H}]_{\text{cal}} = a + b(V - V_{\text{HB}}) + c \Sigma\text{Mg} + d \Sigma\text{Mg}^{-1.5} + e \Sigma\text{Mg}(V - V_{\text{HB}}) \quad (1)$$

where V is the magnitude of the star, V_{HB} is the magnitude of the horizontal branch (HB), and ΣMg is the composite index of the magnesium triplet lines of the star.

Model parameters (a, b, c, d, e) were obtained through least squares minimization method. The presence of numerous local minima in the χ^2 function makes the process strongly dependent on the starting guess parameters. To overcome this, we minimized a penalized χ^2 function of the form:

$$\chi^2 = \frac{(1 - ks)^2 ([\text{Fe}/\text{H}]_{\text{cal}} - [\text{Fe}/\text{H}]_{\text{CaT}})^2}{[\text{Fe}/\text{H}]_{\text{cal}}^2 [\sigma^2([\text{Fe}/\text{H}]_{\text{cal}}) + \sigma^2([\text{Fe}/\text{H}]_{\text{CaT}})]} \quad (2)$$

where ks is the Kolmogorov-Smirnov statistic resulting from comparing the $[\text{Fe}/\text{H}]_{\text{cal}}$ and $[\text{Fe}/\text{H}]_{\text{CaT}}$ metallicity distributions. $[\text{Fe}/\text{H}]_{\text{cal}}$ is the metallicity derived using equation (1) and $[\text{Fe}/\text{H}]_{\text{CaT}}$ is the metallicity of the star obtained through CaT spectroscopy. Their uncertainties are $\sigma([\text{Fe}/\text{H}]_{\text{cal}})$ and $\sigma([\text{Fe}/\text{H}]_{\text{CaT}})$, respectively. We minimized expression (2) using the stars present both in the W09 and B08 catalogues, adopting metallicities from the latter as $[\text{Fe}/\text{H}]_{\text{CaT}}$. In order to avoid local minimums we proceeded in two steps. First, we created an $N \times n$ array covering a realistic domain of the N sampled parameters with n values for each parameter. Once the whole domain of starting points has been scrutinized and the total minimum has been found, its N coordinates are used as a starting point for a more refined least squares minimization of (2).

To avoid stars with large errors, or with low S/N, only those with $\sigma(\Sigma\text{Mg}) < 0.08$ were considered. The errors in the metallicities were obtained by propagating the errors in all the quantities implied in the calculation: V , V_{HB} and $\sigma(\Sigma\text{Mg})$. W09 only provide the $\sigma(\Sigma\text{Mg})$ uncertainty. The other uncertainties were obtained by cross-matching the W09 stars with a photometric catalogue covering the whole body of the galaxy (see [del Pino et al. 2015](#), for further information) and assigning to each star its V magnitude and its corresponding error $\sigma(V)$ from the photometry catalogue. This was done after ensuring that the V magnitudes from both catalogues were compatible within errors. The uncertainty in V_{HB} was set to $\sigma(V_{\text{HB}}) = 0.05$. This value is the standard deviation of 50 measurements of V_{HB} over the photometry catalogue in different non-overlapping regions cov-

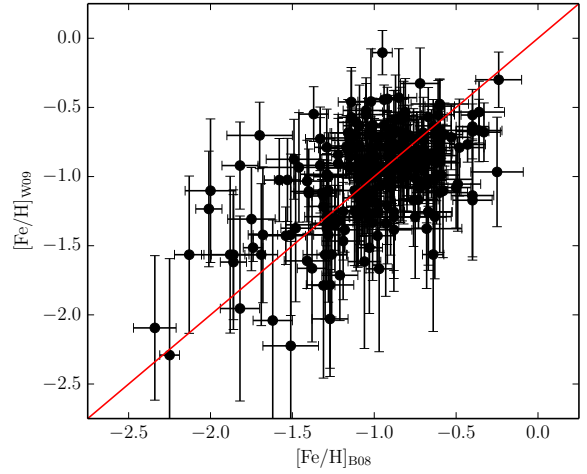


Figure 1. Comparison of metallicities of stars common in the W09 and B08 catalogues after the internal calibration. W09 metallicities have been recalibrated to agree with B08 ones using the [Starkenburg et al. \(2010\)](#) model. The red line indicates the one-to-one correspondence between the two catalogues.

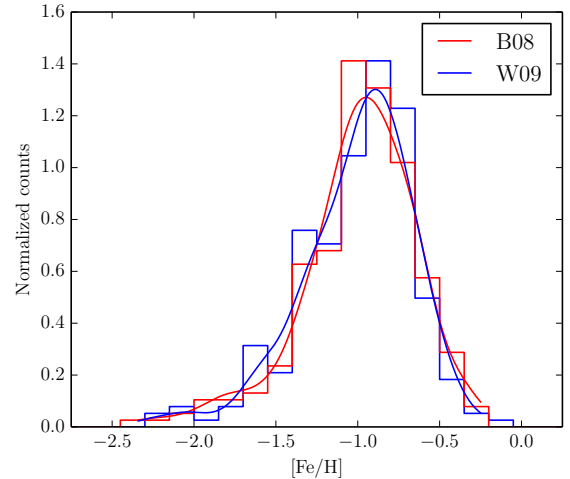


Figure 2. Comparison between metallicity distributions of W09 and B08 stars after the internal calibration. Metallicity distribution of W09 is shown in blue and the one of B08 in red. W09 metallicities have been recalibrated to agree with B08 ones using the [Starkenburg et al. \(2010\)](#) model. Curves represent the fitted distribution functions of metallicities from W09 (blue) and B08 (red).

ering small areas within the whole region spanned by W09 stars.

After the calibration, the metallicity distribution of W09 follows closely the one of B08 so the disagreement seen when considering particular stars becomes smaller when we consider a statistically significant number of stars. In Figure 1 we show a comparison between the metallicities of the stars common to both catalogues after the internal calibration. Figure 2 shows the metallicity distribution of the same stars from W09 and B08 (also after the internal calibration).

A total of 1193 stars from the W09 sample were included

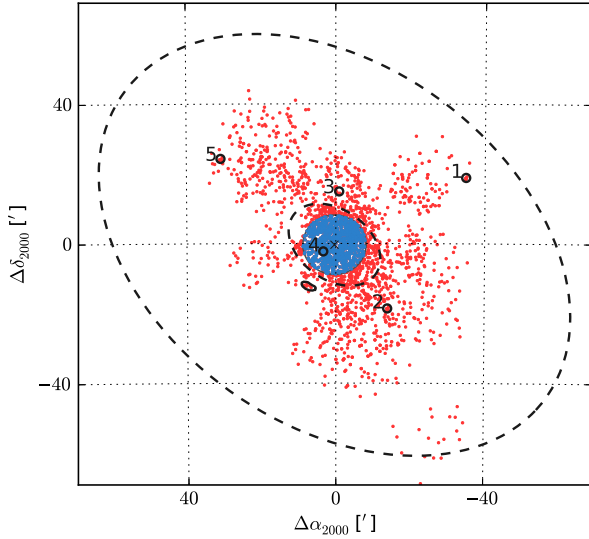


Figure 3. Stars used for the chemo-kinematic analysis of Fornax. These were collected from Pont et al. (2004); Battaglia et al. (2006, 2008b); Walker et al. (2009a); Kirby et al. (2010) and Letarte et al. (2010). The positions of the stars are represented by dots. Blue dots indicate a sub-sample of stars, selected for a consistency test (see Section 5). These are all the stars of the sample lying within a circle of radius $r = 7.7' \sim 300$ pc located at the centre of the galaxy. The dashed ellipses correspond to the core and the tidal radius. The black open circles show the positions of five known globular clusters in Fornax and are labelled accordingly. The position of the inner shell found by Coleman et al. (2004) is marked with a small ellipse at $\Delta\alpha_{2000} \sim 8'$ and $\Delta\delta_{2000} \sim -13'$.

in the final catalogue, which contains the information about the position, metallicity, and v_{LOS} for 2562 stars. The relative positions of the stars in the galaxy are shown in Figure 3. In Figure 4, we show the v_{LOS} map of the whole sample, together with its metallicity distribution and a stripe showing the maximum detected velocity gradient ($\sim 4 \text{ km s}^{-1} \text{ deg}^{-1}$) along the body of Fornax. Note that the direction of this velocity gradient, $\text{PA} = 112 \pm 9 \text{ deg}$, is compatible with the direction of the proper motion vector of Fornax derived by Piatek et al. (2007), $\text{PA} = 127 \pm 4.1 \text{ deg}$ or Walker et al. (2008), $\text{PA} = 120 \text{ deg}$. We believe that this velocity gradient is in fact the projection along the line-of-sight of the transversal proper motion of Fornax and not an intrinsic velocity gradient. In order to have more statistically reliable results in the velocity maps, we have made use of Voronoi tessellation techniques. With this method, an adaptive grid is used instead of a regular one, adjusting the sizes of the cells to keep a constant number of stars within the cells. Areas where there were less observed stars, are covered by larger grid cells. This method was simultaneously used to clean the sample from outliers. The tessellation was performed in an iterative way until convergence, removing from every cell stars lying outside the 3σ of the velocity distribution within the cell.

3 BEACON: A METHOD TO FIND CHEMO-KINEMATIC PATTERNS

Disentangling chemo-kinematic patterns among the stars of a dSph is difficult. There have been numerous attempts of detecting rotation, generally concluding that no strong rotation signal can be found in these systems. Nevertheless, significant rotation signatures have been reported for some dSph galaxies in the literature. Using v_{LOS} measurements for 470 RGB stars Battaglia et al. (2008a) found a small velocity gradient of $7.6^{+3.0}_{-2.2} \text{ km s}^{-1}$ along the projected major axis of the Sculptor dSph galaxy. Furthermore, Lewis et al. (2007) and Fraternali et al. (2009) claimed to have detected a regular rotation around the minor axis in the Cetus and Tucana dSph galaxies with a velocity difference of $\sim 8 \text{ km s}^{-1}$ and $\sim 16 \text{ km s}^{-1}$ respectively. These conclusions were however based on the v_{LOS} measurements for only a few tens of RGB stars in each galaxy which is not enough to derive solid results. More recently, Amorisco & Evans (2012) found a small rotation signal in Fornax using the W09 data set. The small number of dSphs where dynamical patterns have been found together with their relatively weak rotation signals have supported the general idea of dSphs being pressure supported systems. Therefore, their elongated shapes were usually interpreted as a result of tidal interactions with their larger host galaxies.

However, our technological limitations could be, at least in part, responsible for these results. We are only able to obtain spectra of a limited number of individual RGB stars, therefore sampling a very small fraction of the total stellar population of these galaxies. Due to this poor sampling a weak rotation signal could well be hidden in a relatively large velocity dispersion. These observational limitations make it necessary to implement new software techniques to help us find dynamical patterns in these galaxies.

BEACON is a new software tool developed to find groups of stars with similar chemo-kinematic properties. Its scientific objective is to detect possible rotation patterns in resolved stellar populations. It has been written in the Python language and we are currently working to make the code publicly available to the scientific community.

3.1 Basic Definitions

From the point of view of dynamics, galaxies are N -body systems where each star can be defined by its position and velocity. Therefore, the internal dynamics of a galaxy with N stars can be described by a state vector, $\mathbf{x} \in \mathbb{R}^{6N}$, where $\mathbf{x} = (\mathbf{r}_1 \dots \mathbf{r}_N, \mathbf{v}_1 \dots \mathbf{v}_N)$ and each $\mathbf{r}_1 \dots \mathbf{r}_N, \mathbf{v}_1 \dots \mathbf{v}_N \in \mathbb{R}^3$.

The most important issue that observational astronomers have to deal with is the fact that observations only provide information about the projection of this state vector in 3 out of 6 coordinates and obviously not for all the N stars of the system but only for a small observed fraction, n . These 3 coordinates usually are the classical coordinates RA, Dec, and v_{LOS} , which are, respectively, the projection of the position on to the celestial sphere and the projection of the velocity on to the line of sight: $\mathbf{x}^p = (\mathbf{r}_1^p \dots \mathbf{r}_n^p, \mathbf{v}_1^p \dots \mathbf{v}_n^p)$ where the superscript p stands for ‘projected’.

These pieces of information are insufficient to unequivocally determine the dynamical state of a galaxy, but allow us to make some inquiries through assumptions or models. The

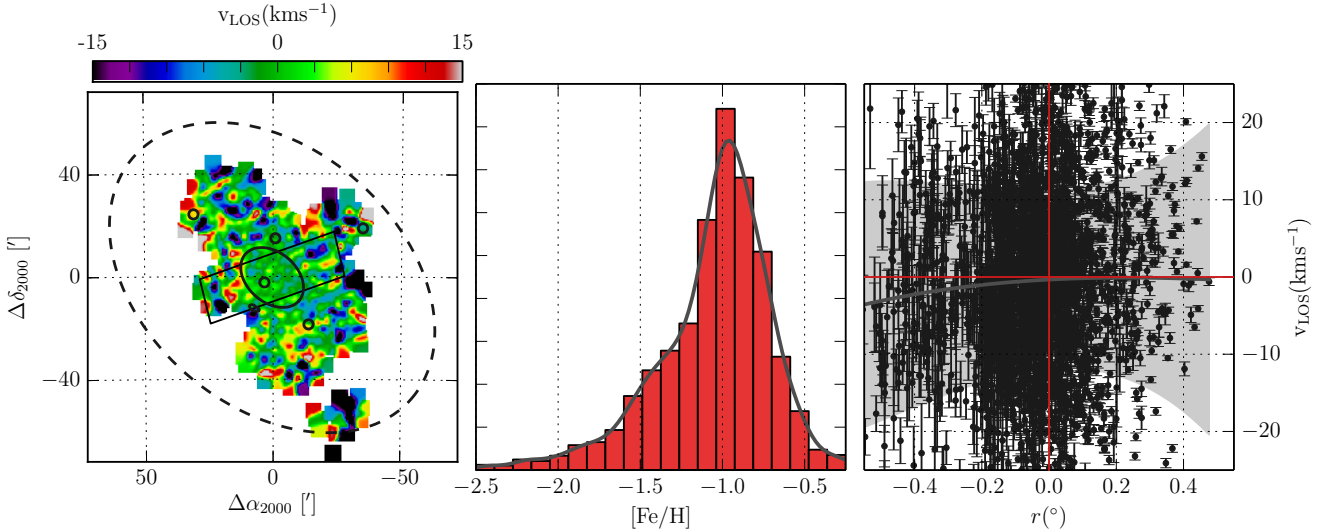


Figure 4. The map of line-of-sight velocities, v_{LOS} for the 2562 stars used in the present work. The left panel shows the v_{LOS} as a function of position. The core and the tidal radius are represented by dashed ellipses. Empty circles indicate the positions of globular clusters in Fornax. The middle panel plots the metallicity distribution of the stars shown in the left panel. The right panel shows the velocities of the stars along the stripe marked in the left panel. The average velocity along the stripe is shown by a grey line, while its dispersion is represented by the shaded area. Voronoi tessellation techniques were used in order to obtain a constant number of stars per grid cell.

first and most important model to be considered is the one assuming that the system should be in virial equilibrium and is kinematically supported. Stars should be orbiting around the centre of mass (CM) of the galaxy with trajectories that follow a common rotation pattern (rotation supported systems) or are randomly oriented (pressure supported).

Disentangling kinematic patterns becomes difficult when using only the projection of the state vector of a reduced sample of stars. To improve our knowledge about the state of each star, one more assumption can be imposed: we can suppose that stars showing similar kinematic patterns should also have similar chemical composition. The latter assumption is based on the idea that stars would conserve the kinetic properties of the gas cloud from which they were formed. In the following, we will concentrate on distinguishing possible rotation patterns using a state vector defined as $\Phi = (\mathbf{r}_1^p \dots \mathbf{r}_n^p, \mathbf{v}_1^p \dots \mathbf{v}_n^p, Z_1 \dots Z_n)$, where Z_i are the metallicities of the stars.

3.2 BEACON in a nutshell

3.2.1 Outline of the procedure

Finding streams of material with similar chemo-kinematic patterns can be mathematically expressed as a hierarchical clustering problem. This can be addressed via different approaches, for example the Bayesian techniques of Amorisco & Evans (2012). In the present work, we propose a completely different strategy. We have developed a software suite called BEACON which has been optimized for joining together groups of stars with similar positions, velocities and metallicities. The core of BEACON is based on the OPTICS algorithm by Ankerst et al. (1999) and can be divided into the following steps:

1. Building the state vector Φ ;
2. Clustering process of Φ ;
3. Analysis of clusters;
4. Recovering the original coordinates of clustered stars;
5. Uniqueness of solutions and groups creation.

In the following we provide a description of each step:

1. Building the state vector Φ : Having measurements for n stars, we have to create a convenient state vector which represents our sample. In this vector, we may include any coordinate providing information of interest about the state of the stars: positions, v_{LOS} and metallicities. Positions and velocities of stars are transformed into the galaxy CM rest frame of reference (RA^{CM} , Dec^{CM} , $v_{\text{LOS}}^{\text{CM}}$) and for convenience position coordinates are converted into polar coordinates defined as (r, θ) . Since the orbits followed by the streams of stars do not have to be perfectly circular, r should be a free parameter and should not to be included in Φ . The latter decision changes the possible usages of BEACON. For example, including r would make BEACON more sensitive to streams or clumps of stars more concentrated in the space defined by Φ , but less effective in detecting more general chemo-kinematical patterns. Since our objective is to study general rotation patterns in the galaxy, we did not include r in Φ .

All quantities can be standardized before the clustering process. Standardization of input variables will normalize the relative weight of each of them during clustering. This allows us to avoid undesirable effects related to the dynamical range covered by the variables involved in the clustering process. For example, we wish to avoid the situation when the v_{LOS} , which can take values from the range of almost $\pm 25 \text{ km s}^{-1}$ weights much more than the metallicity, $[\text{Fe}/\text{H}]$, which only covers ~ 0.008 in dex scale. In case it was required, standardization to standard deviation, dynamical

range and the variance of variables are all included in the code.

After the process, the state vector would have the explicit form of:

$$\Phi = \begin{bmatrix} \theta_1 & v_{\text{LOS},1} & Z_1 \\ \theta_2 & v_{\text{LOS},2} & Z_2 \\ \vdots & \vdots & \vdots \\ \theta_n & v_{\text{LOS},n} & Z_n \end{bmatrix} \quad (3)$$

where each θ_i is the angular coordinate of the i^{th} star with respect to the CM and the optical minor axis of the galaxy and each $v_{\text{LOS},i}$ is measured with respect to the $v_{\text{LOS}}^{\text{CM}}$.

2. Clustering process of Φ : BEACON will then create a new state vector, symmetrical in relation to Φ in coordinates and velocities with respect to the centre of the galaxy. Both vectors are stacked into a unique vector Θ containing $2n$ stars:

$$\Theta = \begin{bmatrix} \theta_1 & v_{\text{LOS},1} & Z_1 \\ \vdots & \vdots & \vdots \\ \theta_n & v_{\text{LOS},n} & Z_n \\ \theta_1 + \pi \pmod{2\pi} & -v_{\text{LOS},1} & Z_1 \\ \vdots & \vdots & \vdots \\ \theta_n + \pi \pmod{2\pi} & -v_{\text{LOS},n} & Z_n \end{bmatrix} \quad (4)$$

This Θ vector is the input for the OPTICS algorithm. The use of Θ instead of Φ allows us to cluster stars with similar symmetrical positions (θ and $\theta + \pi$), which are moving with similar velocities but in the opposite direction (v_{LOS} and $-v_{\text{LOS}}$).

3. Analysis of clusters: Once the stars have been clustered, BEACON searches in each cluster for stars located at both sides of the CM of the galaxy. We define ϵ as the ratio of the numbers of stars at one and at the other side of the CM. If ϵ is greater than a certain critical quantity, ϵ_c , the cluster is catalogued as a possible circular or both side stream (BSS). On the other hand, if all stars are on one side of the CM ($\epsilon_c = 0$), the cluster is catalogued as a possible one side or non-circular stream (OSS). Clusters with $0 < \epsilon < \epsilon_c$ are dismissed.

4. Recovering the original coordinates of clustered stars: The original coordinates, containing the real physical data, of the stars clustered in Θ are recovered from Φ .

5. Uniqueness of solutions and groups creation: In this last step, BEACON checks whether common stars between clusters exist, and applies uniqueness criteria. Two alternative uniqueness criteria are implemented: *all elements* or *any element*. The former considers two clusters as different groups if they differ by at least one star. The latter criterion considers clusters sharing any stars as coming from the same group and merges them all into one group.

3.2.2 Additional parameters

Apart from the observational data, some additional information is required in order to perform the clustering. Such information is used to create the reference frame centred on the CM of the galaxy (*galaxy parameters*) and to control the clustering process (*clustering parameters*).

In order to work properly, BEACON needs the aforementioned parameters as input. The *galaxy parameters* are the

Table 2. Clustering parameters

Quantity	Value
MCS	[13, 28]
ϵ_c	1/3
<i>Standardization Method</i>	Standard deviation
<i>Uniqueness Criteria</i>	Any element

coordinates of the CM. More data can be provided, but only the position and the v_{LOS} of the CM (RA^{CM} , Dec^{CM} , $v_{\text{LOS}}^{\text{CM}}$) are strictly needed. These coordinates allow BEACON to create the reference frame centred on the CM, which is necessary in order to detect rotation patterns in the galaxy. The *clustering parameters*, on the other hand, are a collection of parameters defining the clustering criteria. Some of them are the *standardization method*, the *uniqueness criteria* and the *minimum cluster size* (MCS). These have to be tuned for the specific galaxy under study and depend for example on the number of sampled stars, the completeness of the sample and its spatial coverage.

3.3 The case of Fornax: optimal parameters

For the analysis of Fornax, we initially adopted the galaxy parameters listed in Table 1. On the other hand, the *clustering parameters* were fine-tuned through several tests. In these tests we analyzed the solutions of BEACON as a function of variations in the clustering parameters.

The *standardization method* affects the relative importance of each coordinate during the clustering. In principle, nothing suggests that any coordinate should have a larger weight than any other in the clustering process. Therefore we applied a standard deviation standardization. This method assigns the most balanced weight to the three coordinates (θ , v_{LOS} , and Z). Also the *uniqueness criteria* were set to ‘any element’, in order to avoid duplicities in stars.

Once the standardization and the uniqueness parameters are fixed, we can study how the number of groups is affected by the MCS parameter. The MCS parameter is the minimum number of stars that a cluster should have in order not to be rejected during the process. It has a direct impact on the final number of groups resulting from the study. Figure 5 shows the number of groups found by BEACON as a function of the MCS parameter. Optimal values were found in the range of $13 < \text{MCS} < 28$, which are such that the derivative of a fitted negative exponential $f'(\text{MCS}) = -a b \exp(-b \text{MCS})$ is between -1 and -0.5 . Below $\text{MCS} = 13$, detection rates increase rapidly with a small decrease in the MCS parameter, indicating possible false detections. On the other hand, individual group detections drop rapidly to the general rotation pattern of the galaxy for values greater than $\text{MCS} = 28$, not allowing us to analyze the finer details. A more detailed explanation concerning this choice, and the influence of the MCS parameter on the final results can be found in Sections 4.1 and 5. The *clustering parameters* finally used are listed in Table 2.

BEACON has been designed to find chemo-kinematic patterns which differ from the general kinematic behaviour of the stellar system. Therefore, it is unlikely to find large

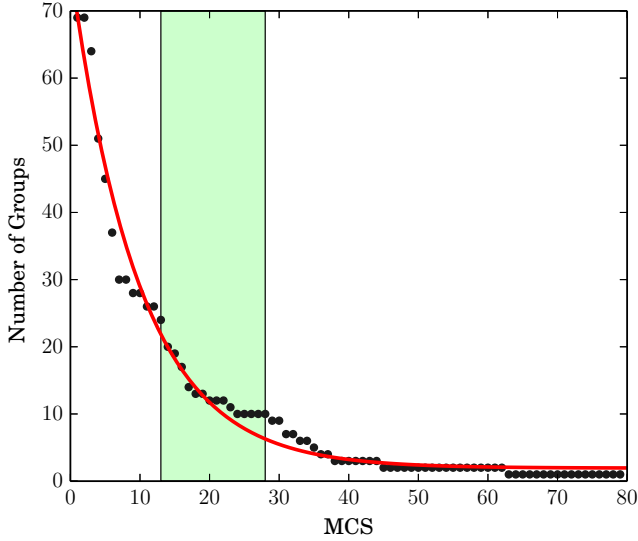


Figure 5. Number of resulting circular streams as a function of *minimum cluster size* parameter (MCS). The red line shows an exponential function fitted to the points. The area of the preferred values for MCS is marked in green ($13 < \text{MCS} < 28$).

scale kinematics patterns affecting the whole galaxy i.e. a general rotation pattern or entirely random kinematics. This is due to the way clusters are formed in the Φ space, where general kinematic patterns involving all stars regardless of their metallicity represent a continuous cloud of points. This is the case of proper-motion induced gradients, such as the one found in Section 2.2, which was discarded by BEACON, and not taken into account in the subsequent analysis.

3.4 Derivation of galaxy parameters using BEACON

Stars in a galaxy in equilibrium should be rotating around the CM of the galaxy. Therefore, BEACON is expected to find more BSSs and less OSSs around this CM. Using this idea, BEACON can be applied to find the best *galaxy parameters*, i.e. the CM coordinates. This is independent of the chosen *clustering parameters* and can be done by maximizing the number of BSSs and minimizing the OSSs as a function of the *galaxy parameters*.

The procedure is as follows. A grid of coordinates is generated centred on the commonly adopted coordinates for the galaxy: RA^{gal} , Dec^{gal} and $v_{\text{LOS}}^{\text{gal}}$. Each set of coordinates from this grid is used as input *galaxy parameters* for BEACON. The number of both, BSSs and OSSs, is stored in a data cube of the same dimension as the coordinates grid. The coordinates of the CM should correspond to the point of the grid producing the largest number of BSSs and the smallest number of OSSs. We quantify this requirement defining:

$$\mu(\text{RA}^{\text{CM}}, \text{Dec}^{\text{CM}}, v_{\text{LOS}}^{\text{CM}}) = \frac{(|\text{BSSs}| + 1)^2}{(|\text{OSSs}| + 1)^2} \quad (5)$$

where $|\text{BSSs}|$ is the number of BSSs and $|\text{OSSs}|$ is the number of OSSs found for the coordinates $(\text{RA}^{\text{CM}}, \text{Dec}^{\text{CM}}, v_{\text{LOS}}^{\text{CM}})$.

In the case of Fornax, we used the values listed in Table 1 as central values for generating the grid of coordinates with $150 \times 150 \times 200$ steps in RA, Dec, and v_{LOS} respectively.

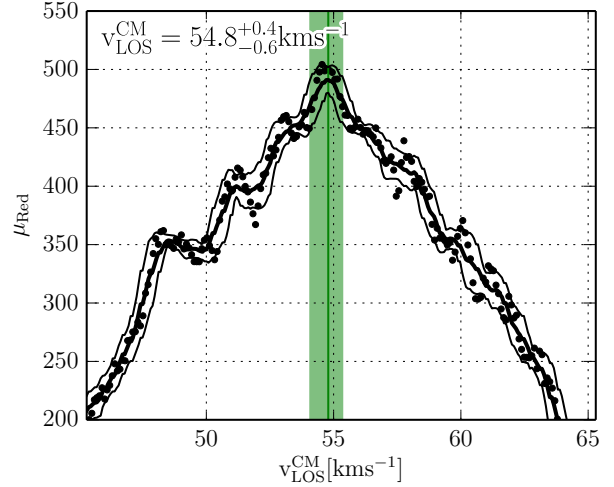


Figure 6. μ_{red} as a function of $v_{\text{LOS}}^{\text{CM}}$ for Fornax. The average value of μ_{red} and its dispersion are shown by the black thick and thin curves respectively. The peak of the distribution is marked by the vertical green line while its dispersion is shown with the shaded area.

The value of μ was calculated using BEACON for each of the 4.5×10^6 grid coordinate sets. This provided the probability distribution map of the CM coordinates.

A two-dimensional Gaussian profile was then fitted to each $\mu(\text{RA}^{\text{CM}}, \text{Dec}^{\text{CM}}, v_{\text{LOS},k}^{\text{CM}})$ distribution map, with $0 \leq k \leq 199$. We define a ‘reduced’ μ , $\mu_{\text{red}}(v_{\text{LOS}}^{\text{CM}})$, as the height of the fitted Gaussian. This definition allows us to find the $v_{\text{LOS},k}^{\text{CM}}$ which produces the highest density of favourable results, i.e. the maximum of $|\text{BSSs}|$ and the minimum of $|\text{OSSs}|$. Results of this procedure are shown in Figure 6.

We applied a box-car average with a bin width of 0.6 km s^{-1} (the typical error in v_{LOS} of our sample) in 256 steps over $\mu_{\text{red}}(v_{\text{LOS}}^{\text{CM}})$. This resulted in a value $v_{\text{LOS}}^{\text{CM}} = 54.8^{+0.4}_{-0.6} \text{ km s}^{-1}$ for Fornax, which is in good agreement with results of other authors (Mateo et al. 1991; Walker et al. 2006). We then constructed $\mu'(\text{RA}^{\text{CM}}, \text{Dec}^{\text{CM}})$ by integrating $\mu(\text{RA}^{\text{CM}}, \text{Dec}^{\text{CM}}, v_{\text{LOS}}^{\text{CM}})$ in the $v_{\text{LOS}}^{\text{CM}}$ direction:

$$\mu'(\text{RA}^{\text{CM}}, \text{Dec}^{\text{CM}}) = \int_{v_1}^{v_2} \mu(\text{RA}^{\text{CM}}, \text{Dec}^{\text{CM}}, v_{\text{LOS}}^{\text{CM}}) dv_{\text{LOS}}^{\text{CM}} \quad (6)$$

where $v_1 = v_{\text{LOS}}^{\text{CM}} - \sigma(v_{\text{LOS}}^{\text{CM}})$ and $v_2 = v_{\text{LOS}}^{\text{CM}} + \sigma(v_{\text{LOS}}^{\text{CM}})$. The resulting map is shown in Figure 7. Two possible centres of rotation were found near the optical centre of the galaxy. The most important one is located roughly at the optical centre given by van den Bergh (1999). The other centre was identified at $\sim 4'$ to the south of the optical centre. This may indicate that the galaxy has recently accreted some material which is still not in equilibrium.

We have determined the best *galaxy parameters* for Fornax by fitting $\mu'(\text{RA}^{\text{CM}}, \text{Dec}^{\text{CM}})$ with a single Gaussian profile and a profile composed of two Gaussians. The results are listed in Table 3. The two-Gaussian profile clearly fits the data better. This profile can be used to obtain μ_{red} resulting in two preferred velocities for each CM. The one coinciding with the optical centre of the galaxy has a velocity of $v_{\text{LOS},1}^{\text{CM}} = 55.5^{+0.5}_{-0.8} \text{ km s}^{-1}$, while the secondary centre shows

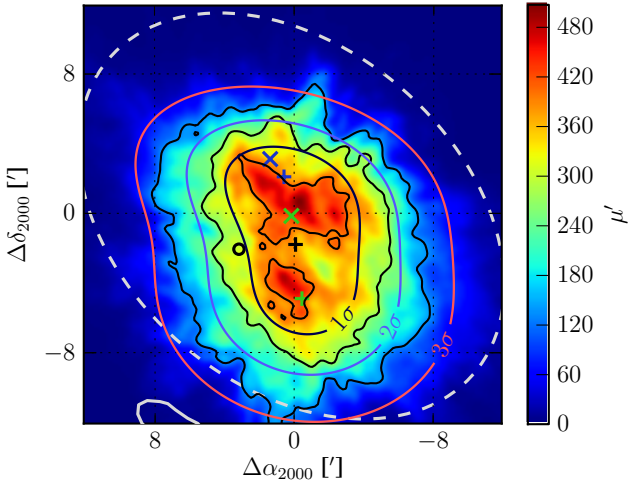


Figure 7. Probability density map of the location of the CM of Fornax. The color scale represents the value of $\mu'(\text{RA}^{\text{CM}}, \text{Dec}^{\text{CM}})$. Contours correspond to the 3σ , 2σ and 1σ differences in standard deviation units with respect to the best solution found with two Gaussians. The centres of the two-Gaussian fits are represented by the blue and green + signs, respectively for (1) and (2). The centre obtained from fitting a single Gaussian profile is represented by the black + sign. The core radius is shown by the light gray dashed ellipse, while the globular cluster Fornax 4 is indicated by the empty circle. The inner clump of stars found by Coleman et al. (2004) is shown at $\Delta\alpha_{2000} \sim 8'$, $\Delta\delta_{2000} \sim -10'$. Two optical centres have been plotted with the \times signs: the one by Mateo (1998) in blue and the one derived by (van den Bergh 1999) in green.

a systemic v_{LOS} of $v_{\text{LOS},2}^{\text{CM}} = 54.5_{-0.6}^{+0.7} \text{ km s}^{-1}$. This difference is not significant (within 1σ), although this refers to only one of the three velocity components. We do not have information about the transversal components. On the other hand, the fact that the projected positions of both CM are statistically different, may indicate the presence of at least two dynamically decoupled components in the galaxy.

3.5 The age of the stars

The existence of an AMR in Fornax has been demonstrated photometrically and spectroscopically in several works (see for example Pont et al. 2004; Battaglia et al. 2006; Coleman & de Jong 2008; de Boer et al. 2012; del Pino et al. 2013; Piatti et al. 2014). In principle, this allows us to assign an average age to each group of stars based on their metallicity. Several methods exist to derive the ages of spectroscopically measured stars. Carrera et al. (2008a,b) made use of polynomial relationships in order to obtain the approximate age of each star. In this paper however, we will use probability distribution functions (PDFs) of the metallicity distribution in each group and fit these to our observed AMR of Fornax. The reason to do so is the lack of precision in the metallicity measurements for a given star, which is however not a strong obstacle when considering the metallicity distribution of the whole group. The procedure is described below.

For each star in a group, we created 2×10^3 synthetic stars with metallicities chosen randomly from a Gaussian

probability distribution with a mean value equal to the metallicity of the star, Z_i , and dispersion σ equal to the metallicity error $\sigma(Z_i)$. In this way, we have a distribution of $2n \times 10^3$ stars for the whole group, where n is the number of stars in the group.

We constructed a PDF for the AMR based on the three SFHs derived in del Pino et al. (2013). We created an average SFH of the three SFHs normalized to the integral over time of their star formation rate $[\psi(t)]$. From this averaged SFH, we created a discrete AMR over 5×10^3 age steps linearly distributed between 2 Gyr and 13.5 Gyr (we do not expect RGB stars younger than 2 Gyr). In each one of these age steps, we created a distribution of 10^4 stars, following the PDF derived from the SFH at that age. This created a total of 5×10^7 stars, in 5×10^3 metallicity distributions following the metallicity distributions of the SFH at the corresponding age. The procedure ends by comparing the metallicity distribution for each group with the 5×10^3 metallicity distributions generated from the SFH. The comparison was made through a Kolmogorov-Smirnov (K-S) test and the results were stored for each group and age step.

In order to avoid stochastic sampling variations in the results, the whole procedure was repeated 1000 times. For each group, the resulting p -values of the K-S test turned out to be normally distributed around a central age value. The adopted age of each group is therefore the mean value of the normal distribution of all its assigned ages and the assigned error is the standard deviation of this distribution.

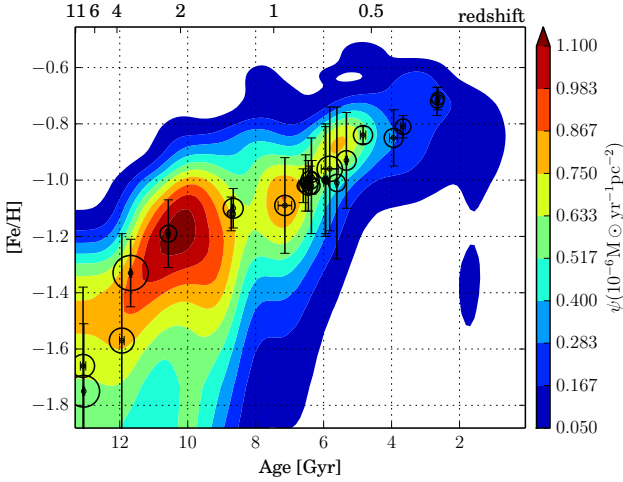
4 RESULTS

After applying BEACON over our catalogue of 2562 stars, a total of 985 of them were classified into 24 possible circular streams. No non-circular streams were detected. The 1577 remaining stars were considered as stars which do not follow any strong chemo-kinematical pattern. Some of these stars may belong, in fact, to rotating streams and have been misclassified due to the lack of 3D kinematic information for them. For example, stars with circular orbits and projected positions close to their rotation axis will show nearly zero v_{LOS} , making their classification into BSSs difficult. Some other may simply belong to badly sampled populations that have not fulfilled the minimum requirements to be considered as a group. Still, the fact that $\sim 60\%$ of the stars were not classified into BSS indicates that Fornax is dominated by entirely random kinematics. This is the expected result for a pressure supported dSph galaxy, and does not rule out the presence of rotating stellar populations in the galaxy.

We derived the age for each BSS following the method described in the previous section. The typical uncertainty provided by this method is of the order of 0.05 Gyr, much smaller than the intrinsic error associated to the SFH of Fornax (del Pino et al. 2013), and other possible sources of error not discussed in this paper. For this reason we do not expect precision higher than ~ 2 Gyr at oldest ages, and no better than ~ 0.7 for ages around 3 Gyr. The ages obtained here provide therefore an insight on the sequence of events associated with the different clusters found by BEACON, allowing us a direct comparison with the SFH of Fornax. The averaged AMR of Fornax, obtained from the SFH derived in del Pino et al. (2013) and the BSS groups with their assigned

Table 3. Tuned galaxy parameters for the Fornax dSph.

Model	RA ^{CM} (J2000)	Dec ^{CM} (J2000)	v _{LOS} ^{CM} [km s ⁻¹]
Single-Gaussian	2h 39m (51.93 ± 0.02)s	−34° 31′ (54.1 ± 0.4)″	54.8 ^{+0.4} _{−0.6}
Two-Gaussian (1)	2h 39m (55.1 ± 0.1)s	−34° 28′ (1 ± 2)″	55.5 ^{+0.5} _{−0.8}
Two-Gaussian (2)	2h 39m (50.14 ± 0.05)s	−34° 35′ (1 ± 3)″	54.5 ^{+0.7} _{−0.6}

**Figure 8.** Averaged SFH used to derive the ages of the BSSs. Each BSS is represented by a circle of size proportional to its angular momentum modulus. Vertical error bars show the metallicity dispersion of each BSS.

ages are shown in Figure 8. In addition to the age, a set of other useful properties can be derived for each BSS. Some of these quantities are listed in Table 4. In the following we discuss each of them separately.

4.1 The angular momentum

Probably the most interesting property which can be derived for each BSS is the projected angular momentum, $\mathbf{L} = \sum_{i=1}^{i=j} \mathbf{r}_i \times m_i \mathbf{v}_i$, where m_i is the mass of the i^{th} star and j is the number of stars in the BSS. A priori, we do not have information about the homogeneity of our sample in terms of metallicity. A sensible way to avoid sampling effects is to normalize the \mathbf{L} vector of every group to the number of stars in the group. This is roughly the same as expressing the angular momentum per unit of stellar mass and provides a measure of the mean momentum \mathbf{p} of the stars forming a BSS. In the following we will use only quantities normalized in this way to the number of stars in each BSS.

Figure 9 shows the angular momenta \mathbf{L} for the 24 BSSs found using MCS = 13 and the 10 BSSs found adopting MCS = 28. The resulting \mathbf{L} show a clear preferred orientation. While the low-metallicity BSSs tend to rotate around the minor axis of the galaxy, the more metal rich ones appear to have more random patterns of rotation. Low-metallicity

Table 4. Mean properties of circular streams detected in Fornax.

SC	[Fe/H]	L [10 ³ pc ² s ⁻¹]	θ [°]	Age [Gyr]
1	−1.75 ± 0.24	14.0 ± 0.5	172 ± 2	13.06 ± 0.03
2	−1.66 ± 0.28	7.3 ± 0.3	174 ± 1	13.08 ± 0.08
3	−1.57 ± 0.38	8.6 ± 0.2	344.5 ± 0.9	11.94 ± 0.07
4	−1.33 ± 0.12	17.2 ± 0.7	175 ± 3	11.68 ± 0.03
5	−1.19 ± 0.12	3.91 ± 0.08	17.5 ± 0.7	10.57 ± 0.04
6	−1.12 ± 0.06	0.871 ± 0.008	358.5 ± 0.2	8.72 ± 0.02
7	−1.10 ± 0.07	5.5 ± 0.1	167.9 ± 0.4	8.66 ± 0.02
8	−1.09 ± 0.17	5.7 ± 0.3	302 ± 3	7.14 ± 0.20
9	−1.02 ± 0.06	2.02 ± 0.07	350.2 ± 0.6	6.60 ± 0.03
10	−1.01 ± 0.10	1.56 ± 0.06	337.8 ± 0.6	6.53 ± 0.04
11	−1.02 ± 0.09	4.9 ± 0.2	172 ± 1	6.45 ± 0.03
12	−1.00 ± 0.05	4.6 ± 0.2	9.7 ± 0.9	6.40 ± 0.02
13	−0.99 ± 0.06	1.4 ± 0.2	98 ± 1	6.34 ± 0.02
14	−1.02 ± 0.17	4.1 ± 0.3	48 ± 2	6.36 ± 0.04
15	−1.00 ± 0.19	0.60 ± 0.01	13.6 ± 0.3	5.94 ± 0.06
16	−1.00 ± 0.20	0.52 ± 0.01	19.0 ± 0.3	5.95 ± 0.03
17	−1.01 ± 0.27	4.1 ± 0.2	218 ± 1	5.61 ± 0.03
18	−0.93 ± 0.17	5.3 ± 0.3	7.3 ± 2	5.33 ± 0.03
19	−0.84 ± 0.03	5.1 ± 0.1	80.7 ± 0.6	4.84 ± 0.08
20	−0.96 ± 0.22	8.9 ± 0.3	25 ± 3	5.8 ± 0.2
21	−0.85 ± 0.10	5.0 ± 0.2	136 ± 1	3.9 ± 0.1
22	−0.81 ± 0.04	3.3 ± 0.1	177.5 ± 0.5	3.66 ± 0.07
23	−0.72 ± 0.05	2.5 ± 0.2	133.4 ± 0.7	2.66 ± 0.03
24	−0.71 ± 0.04	2.2 ± 0.1	343.8 ± 0.5	2.64 ± 0.03

BSSs show larger $|\mathbf{L}|$ in comparison with groups of higher metallicity. The latter can be clearly seen from the projections of the angular momenta on to the main symmetry axes of the galaxy. We will refer to these as a for the major axis and b for the minor axis. The projections are shown in Figure 10. Groups of stars with low [Fe/H] show larger projections of \mathbf{L} on to the minor axis b . This does not mean that metal poor stars rotate faster, because they are also more spatially extended than more metal rich stars.

The alignment of the strongest \mathbf{L} with the main projected optical axes of Fornax is the expected result from the clustering of stars in a rotation-supported system. Interestingly, we observe a small misalignment ($\sim 7^\circ$) between the observed optical minor axis of Fornax and its dominant angular momentum vector. This may indicate that the galaxy is in reality a projected triaxial system, rather than an oblate one (Binney 1985; Weijmans et al. 2014). This is also consistent with the shape expected from N -body simulations of initially disk dwarf galaxies subject to tidal interactions with the Milky Way. As discussed in detail by Lokas et al. (2014b, 2015), the stellar component of such a dwarf galaxy typically transforms into a triaxial (but mostly prolate) bar-

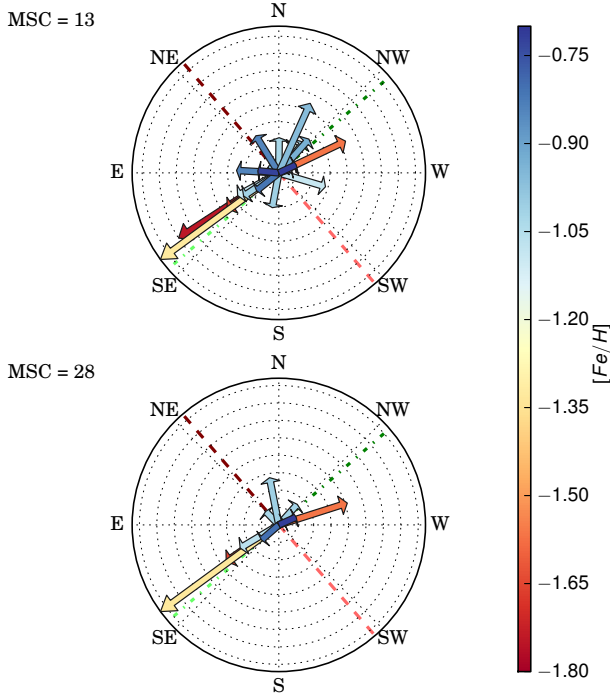


Figure 9. Angular momenta of the different rotating stellar populations in Fornax. Top: the angular momenta \mathbf{L} of the 24 circular streams BSS identified with MCS = 13. Colours represent the mean metallicity of the group. Bottom: same as the top panel, but using MCS = 28. Green dotted-dashed lines represent the orientation of the optical minor axis of the galaxy. The optical major axis is shown by the red dashed lines. Darker colours indicate the positive direction along the axes.

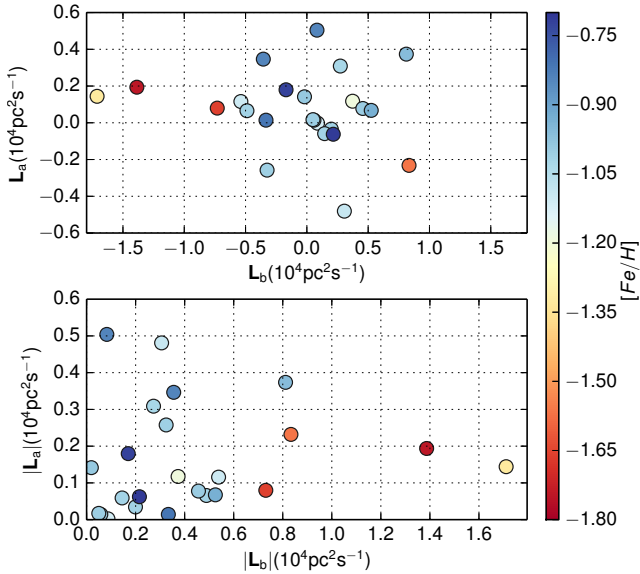


Figure 10. Projection of the angular momenta, \mathbf{L} , on to the major (a) and minor (b) symmetry axes of Fornax for the 24 BSSs. Colours represent the mean metallicity of the groups.

like system at the first pericentre passage. This shape becomes more spherical during the subsequent evolution but remains prolate and retains some rotation around the minor axis.

High-metallicity BSSs gather around relatively low values of L_a and L_b , some of them showing a larger projection on to the major axis of Fornax (prolate rotation). We have defined the positive semi-major and semi-minor axis of Fornax, $+a$ and $+b$ respectively, as the closest to the north. With this definition, we can express \mathbf{L} as the absolute value of the angular momentum and the angle θ with respect to $+b$. In Figure 11 we show the metallicity of each BSS as a function of θ . Different behaviours can be observed as a function of metallicity ($[\text{Fe}/\text{H}]$) and age of the groups. Groups with $[\text{Fe}/\text{H}] \lesssim 1.2$ are older than ~ 10 Gyr and are arranged along $\theta \sim 350^\circ$ and $\theta \sim 170^\circ$ showing small deviations from the minor axis. The BSSs with $-1.2 \lesssim [\text{Fe}/\text{H}] \lesssim -1.0$ exhibit ages from 10 to 6 Gyr. The L s of these groups are more randomly distributed, some of them showing rotation around the north and south direction. The bulk of BSSs we found gather around these metallicities, peaking at $[\text{Fe}/\text{H}] \sim -1.05$. Interestingly, the peak of the metallicity distribution for all the stars in the sample is located at slightly higher metallicities, $[\text{Fe}/\text{H}] \sim -0.95$. In principle, one would expect a peak of detections around the peak of the metallicity distribution of the galaxy. This result indicates that stars with metallicities $[\text{Fe}/\text{H}] \sim -1.05$ show a more singular dynamical pattern. The younger BSSs appear to start to recover the main rotation direction around the minor axis. For the whole galaxy, the preferred orientations of \mathbf{L} are the main axes of the galaxy, especially the minor axis.

We further tested the effects of changing the MCS parameter from 13 to 28. As it can be seen in Figure 9, some groups disappeared or were merged with bigger ones when using MCS = 28. The groups most susceptible to disappear were those with metallicities $[\text{Fe}/\text{H}] \sim -1.05$. This is caused by the more erratic kinematics of the stars at these metallicities. Interestingly, most of the stars in Fornax have metallicities around these values. This discards any possible statistical problem related to the number of stars in our sample around these metallicities. The fact that these groups disappear or rearrange when increasing MCS indicates that stars with $[\text{Fe}/\text{H}] \sim -1.05$ possess, indeed, more chaotic kinematics. This appears to be the reason why it is harder for BEACON to form groups around these metallicity values when using large MCS requirements. On the other hand, reducing MCS will allow BEACON to find numbers of groups showing large variety of kinematics. The three main metal-poor components were always detected by BEACON for values of MCS below 45. These groups represent the most important contribution to the total angular momentum of the galaxy. This result was expected since old, metal-poor stars constitute the majority of stars in Fornax (del Pino et al. 2013). Results for high metallicity groups ($[\text{Fe}/\text{H}] > -0.8$) were also stable and almost independent of the adopted MCS value. All these results are consistent with the odd kinematics shown by the stars with metallicities $[\text{Fe}/\text{H}] \sim -1.05$.

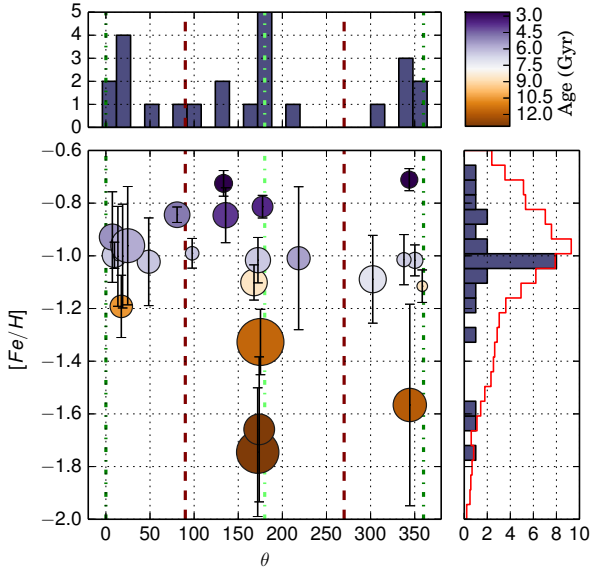


Figure 11. The metallicity, $[\text{Fe}/\text{H}]$, of the BSSs as a function of the orientation, θ , of their angular momenta, \mathbf{L} . Circles represent the BSSs. Their average ages are indicated with a colour scale while the radii of the circles are proportional to $|\mathbf{L}|$. Error bars represent the metallicity dispersion of the groups. Main axes of Fornax are shown by vertical lines. As in Figure 9, the dotted-dashed green lines represent the optical minor axis, while the dashed red ones the major axis. Angles are measured from the positive semi-minor axis of the galaxy, $+b$. Along both axes of the figure we plot histograms showing the distribution of the BSSs as a function of θ and $[\text{Fe}/\text{H}]$. The metallicity distribution of all stars in our sample is drawn with a red line.

4.2 Evolution with time

Estimating the ages of the BSSs allows us to derive the rotation history (RH), $\mathbf{L}(t)$, of Fornax. Considering that time is the most important variable in the problem, we define the RH as an explicit function of it. Formally, $\bar{\mathbf{L}}(t)dt$ is the predominant angular momentum of the galaxy within the time interval $(t, t+dt)$, which can be calculated as the vector sum of all the \mathbf{L}_i of groups with ages within that time interval. To give an estimate of how dispersed the \mathbf{L}_i are from the average rotation axis we defined the dispersion around the mean axis as:

$$\sigma[\bar{\theta}(t)]_{\text{axis}} = \left(\frac{\sum_{i=1}^{i=j} |\mathbf{L}_i| \zeta_i}{\sum_{i=1}^{i=j} |\mathbf{L}_i|} \right)^{1/2} \quad (7)$$

where

$$\phi_i = \begin{cases} \theta_i, & \text{if } |\zeta_i| > \pi/2 \\ \theta_i + \pi \pmod{2\pi}, & \text{if } |\zeta_i| \leq \pi/2 \end{cases} \quad (8)$$

and

$$\zeta_i = \arctan\{\sin[\phi_i - \bar{\theta}(t)], \cos[\phi_i - \bar{\theta}(t)]\}. \quad (9)$$

Therefore $\sigma[\bar{\theta}(t)]_{\text{axis}}$ represents the dispersion of the \mathbf{L}_i within $(t, t+dt)$ around the main axis of rotation $\bar{\mathbf{L}}(t)dt$, independently of the rotation direction.

In order to have statistically reliable results, we used a 1.5 Gyr wide bin, shifting it by 512 small steps within the range of ages found for the BSS. Figure 12 shows the SFH of Fornax derived in [del Pino et al. \(2013\)](#), $\psi(t)$ (first panel),

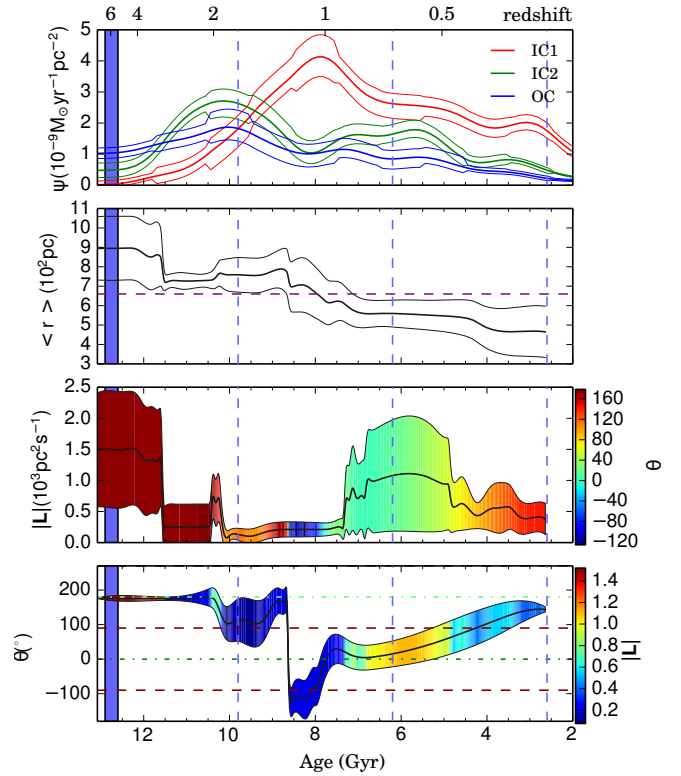


Figure 12. Evolution of preferred angular momentum with time. The first panel shows the SFH of Fornax, derived in [del Pino et al. \(2013\)](#) for the three defined regions (IC1, IC2, OC). The second panel shows the evolution of the mean distance of the stars from the centre of the galaxy, with the present half-light radius (r_h) of Fornax indicated by a horizontal purple dashed line. The third panel shows the evolution of $|\mathbf{L}|$ with time with the colour scale representing the orientation (θ) of \mathbf{L} . The last panel shows the evolution of θ with time with the colour scale representing $|\mathbf{L}|$. As in Figure 9 the dotted-dashed green lines indicate the optical minor axis, while the dashed red ones the major axis. The dispersion of the results is plotted with thinner lines. Possible passages of Fornax through its perigalacticon, derived from the orbital parameters by [Piatek et al. \(2007\)](#), are marked by vertical blue dashed lines. The blue vertical strip in every panel indicates the epoch of reionization.

the mean distance of the stars to the centre of the galaxy, r (second panel), $|\mathbf{L}|(t)$ (third panel), and the angle between $\mathbf{L}(t)$ and $+b$ (fourth panel).

Our results show a clear evolution in the rotation patterns of Fornax. Older stars rotate around the $-b$ axis (the minor axis of the galaxy) with very little dispersion. The value of $\bar{\theta}(t)$ suffers a small variation ~ 10 Gyr ago towards the $+a$ semi-major axis, but afterwards goes back to the initial rotation direction. The most important feature in $\bar{\theta}(t)$ occurs ~ 8 Gyr ago when the galaxy appears to change its preferred rotation direction by $\sim 120^\circ$. This sudden change has small significance because of the low $|\mathbf{L}|(t)$ at this period, but most importantly, this small $|\mathbf{L}|(t)$ can be the consequence of the multiple and more chaotic distribution of θ_i between ~ 10 and ~ 8 Gyr ago. The last ~ 5 Gyr up to 2 Gyr ago show a steady recovery of the original rotation direction.

Fornax shows an important correlation between the most important features of its SFH and its RH. Star formation peaks, located at 10 Gyr ago in the outermost regions (IC2 and OC) and at 8 Gyr ago in the central region (IC1), are accompanied by important changes in the rotation patterns of the galaxy.

The mean distance of the stars from the CM also changes with age. The oldest stars are uniformly spread, even beyond the core radius. As we move to younger populations, these tend to be more concentrated in the central regions of the galaxy. This should be taken into account since the scale length of the population is related to its $|\mathbf{L}|$ momentum. No correlation of $|v_{\text{LOS}}|$ with age was found in the BSS stars, and this indicates that higher $|\mathbf{L}|$ originate from the larger scale length of the old populations.

4.3 Main rotating components

The BSSs can be grouped by their \mathbf{L} s. We applied the OPTICS algorithm over the 24 BSSs, clustering them depending on the direction of their \mathbf{L} . Three main groups were found, each rotating around a different main axis of the galaxy. The results are illustrated in Figure 13.

Interestingly, a different metallicity distribution is found for each preferred direction. The main rotation signal is around the minor axis of the system. The second group of BSSs rotates in the opposite direction, but with larger velocity dispersion. Its metallicity distribution peaks at $[\text{Fe}/\text{H}] \sim -1.1$, with a tail towards lower metallicities, indicating that these stars are at least ~ 8 Gyr old, some of them reaching the oldest ages found in Fornax. The last group shows rotation around the optical major axis of the galaxy (prolate rotation). The metallicity distribution of this group peaks at $[\text{Fe}/\text{H}] \sim -0.9$ and at $[\text{Fe}/\text{H}] \sim -0.7$, which roughly corresponds to stars born ~ 6 and ~ 2 Gyr ago, respectively.

4.4 Rotation curve, orientation and enclosed mass

In Figure 14 we show the rotation curve extracted from the first population of stars in Figure 13. We have selected this group because it is the one which shows the strongest rotation signal.

The detection of rotating components allows, in principle, to derive the enclosed mass as a function of radius. Assuming spherical distribution, the enclosed mass within a radius, r , would be

$$M_{\text{dyn}}(< r) = r(v_c^2 + \sigma^2)/G \quad (10)$$

where G is the gravitational constant, v_c the rotation velocity, and σ the velocity dispersion. At a first approximation, we can associate the v_{LOS} of our clusters to the rotation velocity of the galaxy in order to obtain its mass profile. Using values from Figure 14, we obtained $M(r_{\text{half}}) = 2.5_{-1.5}^{+2.5} \times 10^7 M_\odot$, assuming $r_{\text{half}} = 710 \pm 77$ pc (McConnachie 2012). This value is slightly smaller than those obtained through more classical analyses (Lokas 2009; Walker et al. 2009b; Wolf et al. 2010; Walker & Peñarrubia 2011), but still consistent within 1.5σ with the average of these. On the other hand, we expect our mass to be underestimated due to projection effects. In fact, our measured v_{LOS} would be the projection of v_c along the line-of-sight. Therefore,

$v_c = v_{\text{LOS}}/\cos(\omega)$, where ω is the angle between the rotation plane and the line-of-sight. Assuming an average of these previous results as true value for $M(r_{\text{half}})$, we would need an angle $\omega \sim 50$ deg to reproduce this mass.

5 CONSISTENCY OF THE RESULTS

Our results are subject to a number of observational effects that may bias them. The most important one concerns the spatial coverage of the stars in the sample. If the stars are not uniformly sampled and do not cover the whole body of the galaxy, this can predispose the experiment to find stars with privileged coordinates. In our case, this can be a sensitive matter specially for stars lying outside the galaxy core (see Figure 3), where a clear bias towards the major axis of the galaxy exists.

In order to quantify whether our results can be concentrated around the main axes of the galaxy because of the biased spatial coverage of our sample, we performed the same experiment using only stars located at the very centre of the galaxy, within a circle or radius $r = 7.7' \sim 300$ pc (see Figure 3). This assures a relative isotropy of the sample used in both spatial coordinates (r, θ) . This selection includes approximately 1/3 of the original sample, making it necessary to change the MCS parameter to 5. Despite the reduced number of stars, BEACON still finds groups with rotation preferably around the main axes of the system (see Figure 15). Since at this radius our data are not spatially biased, the fact that the strongest angular momenta are aligned with the main optical axes of the galaxy strongly supports the conclusion that stars indeed move faster around these axes.

A galaxy may be described, at least at some stages of its evolution, as a system of self-gravitating fluid in which geometry and dynamics go hand in hand. If the system has a preferred angular momentum, \mathbf{L} , it will flatten in the direction perpendicular to \mathbf{L} . In fact, assuming a hydrodynamical model for a self-gravitating fluid, one could infer the shape of the galaxy, once its \mathbf{L} is known. The latter dependence supports our conclusion that Fornax is rotating mainly around its main optical axes and that this result is not biased by the spatial coverage of our sample.

The other important source of error in the results are the observational uncertainties of the variables implied in the clustering process. Assuming no errors in the position of the stars, these uncertainties are $\sigma([\text{Fe}/\text{H}])$ and $\sigma(v_{\text{LOS}})$. The effects of these in the final results were calculated from Monte Carlo realizations by stochastically varying the input parameters $[\text{Fe}/\text{H}]$ and v_{LOS} according to Gaussian probability distributions with σ similar to the observational uncertainties of these quantities. The experiment was repeated 10^6 times, obtaining the corresponding BSSs each time. Figure 16 shows the results from the Monte Carlo tests which demonstrate great stability of the results against perturbations in the input variables. Within 3σ , the rotation of Fornax is almost exclusively around the minor axis $-b$, with some weaker rotation around the $+b$ axis. This allows us to conclude that our sample is not biased and that our results are stable.

To check the consistency of results as a function of the clustering parameters, we ran the code adopting different

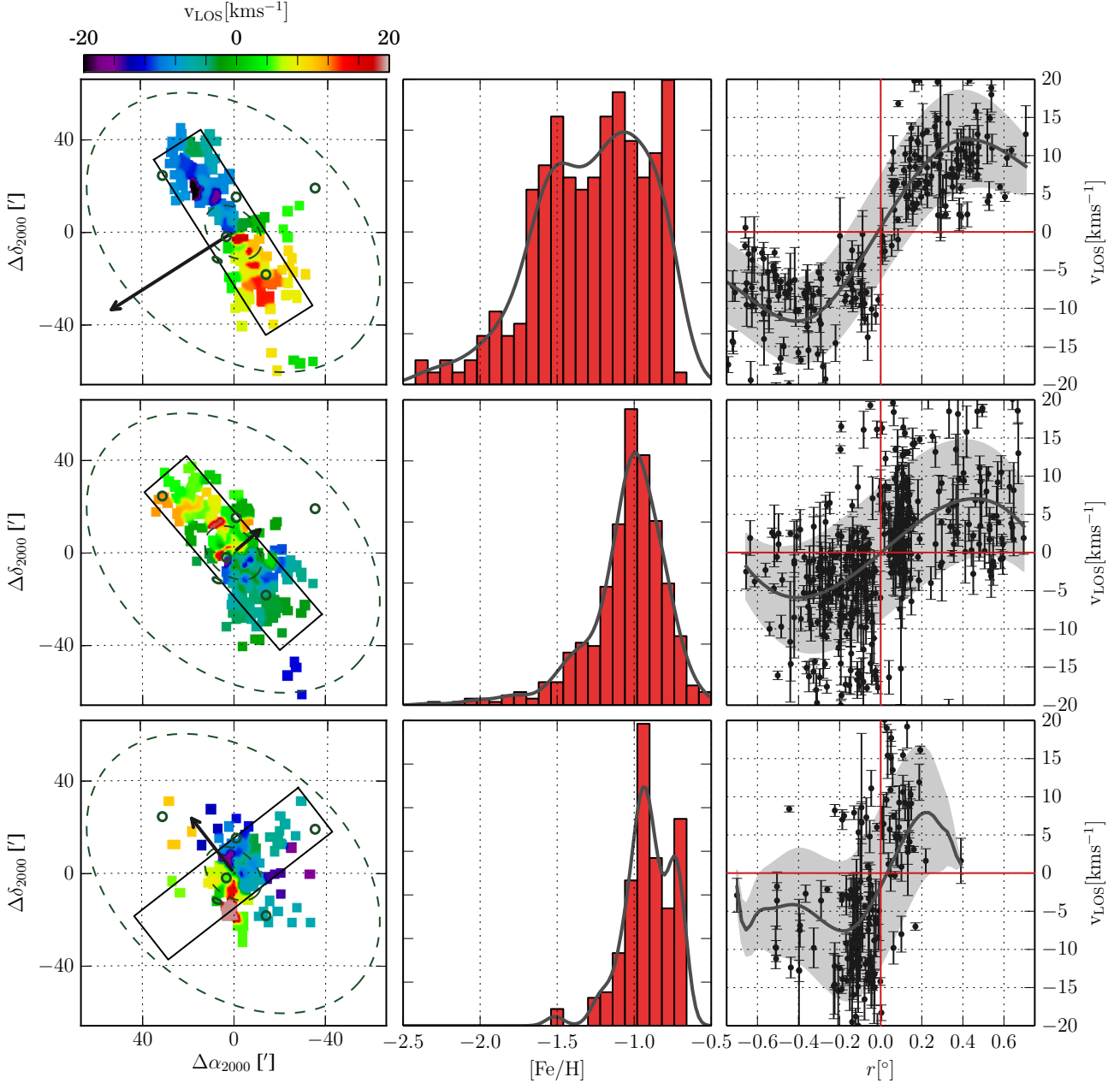


Figure 13. Same as Figure 4, for the different BSSs grouped by their \mathbf{L} . Left panels show the v_{LOS} maps with the black arrow representing \mathbf{L} . Middle panels show the metallicity distribution of the stars shown in the left panels. Right panels plot the velocity of the stars along the stripe shown in the left panels. Results from top to bottom are ordered by the average metallicity of the groups from the lower to higher metallicity. The notation and line types are the same as in Figure 4.

values for MCS. This parameter has the biggest impact on the final results, forcing the code to cluster stars more distant in the space defined by Θ . We tried all possible values between the maximum and minimum optimal values (13 and 28). Results were consistent and qualitatively equivalent, producing less groups as we incremented the MCS parameter, but conserving the general trends in the angular momentum orientation and strength. For example, using MCS = 28 we obtained 10 BSSs which were very similar to the most important ones found with MCS = 13 (see Figure 9). We carefully checked these results using two tests. In the

first one, we crossmatched the stars grouped using MCS = 13 with those using MCS = 28. Only 52 stars were present in the results using MCS = 13 that were not in the ones obtained with MCS = 28. In the latter groups, we found 23 stars that were not common with the stars in groups using MCS = 13. This represents around 7.6% of different stars between both results. As a second test, we divided both results into metal-rich components ($[\text{Fe}/\text{H}] > 1.2$) and metal-poor ($[\text{Fe}/\text{H}] < 1.2$). We compared the average angular momenta and metallicities of these components for the results using both MCS values. No statistically significant differences were

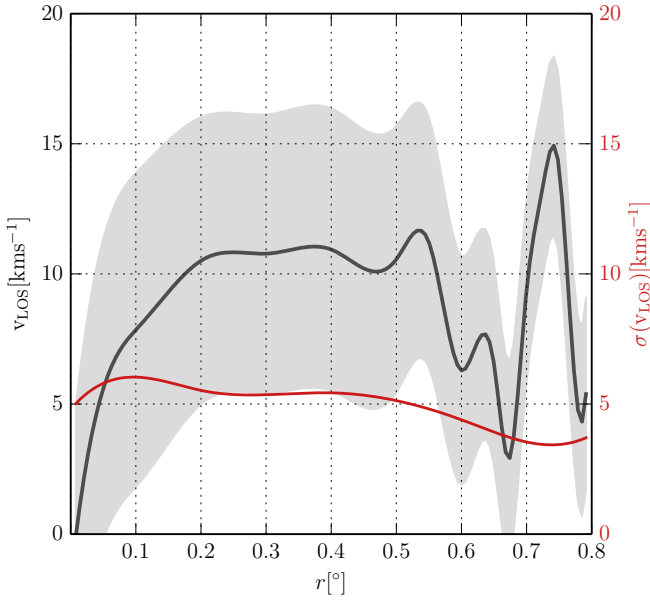


Figure 14. Line-of-sight velocity (v_{LOS}) curve (grey line) for the stars along the stripe shown in the left panel of Figure 13 for the metal poorer population (first one). The spatial coordinate has been inverted, as well as the velocity of the stars in the negative axis of the stripe. The velocity dispersion of these stars is represented by the dashed area and its absolute value by the red curve.

found between the results obtained using MCS 28 or 13. On the other hand, pushing MCS to lower values than 13 produced more stochastic and noisy results. For example, the variations in the clustered stars for the smallest groups (10 stars or less) using MCS = 9 or 10 were found to be around 15%.

Lastly, N -body simulations were used as input for BEACON in order to test how well the software can recover different stellar populations. For this purpose we used the final output of the simulation from Lokas et al. (2014a) aimed to reproduce the Andromeda II dSph galaxy via a merger of two initially disk dwarf galaxies (see also Ebrova & Lokas 2015). The 4×10^5 stars of the simulated galaxy were divided in two different stellar populations with different rotation patterns and metallicities. Specifically, we constructed mock normal metallicity distributions for the two rotating stellar components, one centred at $[\text{Fe}/\text{H}] = -1.3$ and the other at $[\text{Fe}/\text{H}] = -0.9$, with $\sigma = 0.5$ and $\sigma = 0.25$. Several lines of sight were used to create an observational vector Φ of a random selection of 2500 stars containing the projections of the stellar positions on to the sky, the velocities v_{LOS} and metallicities. To make the results more realistic, we simulated artificial errors in v_{LOS} and metallicity using the procedure described in del Pino et al. (2015). For each star, a random value was extracted from a normal distribution centred on the average error of each variable, with the corresponding dispersion.

BEACON succeeded in recovering both populations in a large variety of mock observation set-ups. In the most favourable case of the galaxy observed along its interme-

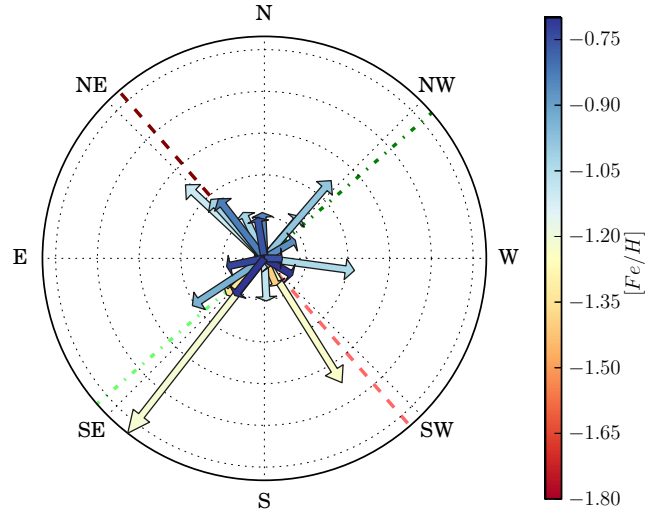


Figure 15. Same as Figure 9 but for stars within a circle of $7.7'$ in radius (see Figure 3). The arrows show the angular momentum vectors, \mathbf{L} , while the colours represent the mean metallicity of the group.

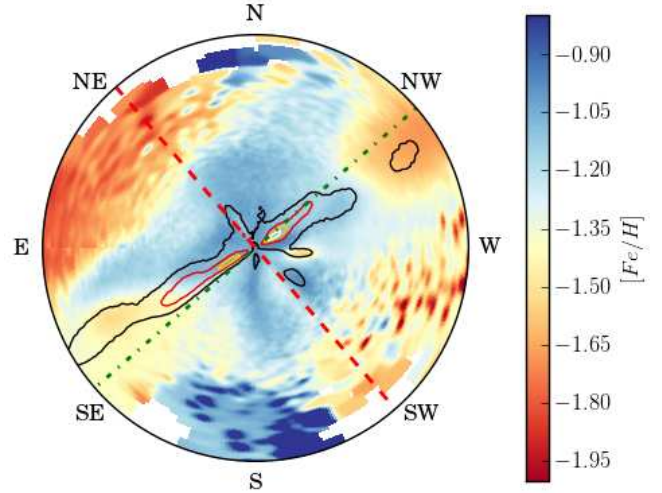


Figure 16. The angular momentum, \mathbf{L} , of Fornax calculated with Monte Carlo error simulations over v_{LOS} and $[\text{Fe}/\text{H}]$ variables. Colours represent the average metallicity while 1σ , 2σ and 3σ contours show the density of the solutions.

diate axis, approximately $\sim 75\%$ of the stars are assigned to streams. Of these, only 1.2% were allocated to the wrong group. In the least favourable case, the galaxy would be observed along the axis of maximum rotation, which for Andromeda II is the longest axis. In this scenario, stars would show $v_{\text{LOS}} \sim 0 \text{ km s}^{-1}$, almost completely losing one of the 4 coordinates. In this case, BEACON assigned approximately 70% of the stars to streams, but with nearly 25% of them badly allocated. This latter scenario is however a very extreme case and unlikely the case for Fornax since we in fact detect rotation. The observation from this point of view is

probably the worst case we can encounter, and would require proper motions measurements in order to improve the results. Further tests of BEACON using N -body simulations will be discussed in a follow-up paper.

6 DISCUSSION

Stars in Fornax show a large variety of orbits which appear to follow certain kinematical patterns. Disentangling these patterns is difficult with only partial information usually available to observers. BEACON has demonstrated to be very powerful in this task, being able to detect reliable chemo-kinematic patterns. Our results show that Fornax rotates, and it has quite complex rotation patterns.

Fornax shows a non-negligible rotation signal ($\sim 2\sigma$ over $v_{\text{LOS}} = 0$), mostly around its optical minor axis (Figure 14). As has been already discussed in Sections 4.1, 4.4 and 5, this is consistent with Fornax being a triaxial system, at least partially supported by rotation.

There exist several mechanisms that could produce a spheroidal galaxy from a progenitor galaxy with a different shape. These include tidal stirring, star formation and supernova feedback or mergers between dwarf galaxies. We believe that a more precise age determination than the one achieved in this work is required in order to derive strong conclusions related to the specific moments in which Fornax could have suffered from any external event, i.e. interaction with other systems. However, we think it is illustrative to make an outline of the properties of Fornax that could be related to these interactions.

Tidal interactions with the MW could be responsible of reshaping a disk galaxy into a dSph. These have been studied in detail by means of high resolution N -body simulations (Mayer et al. 2001; Klimentowski et al. 2009; Kazantzidis et al. 2011; Lokas et al. 2011, 2012). In such controlled experiments, a primordial late type galaxy is placed on an orbit around a MW-like galaxy and evolved for a significant fraction of the Hubble time. Results show that with tight enough orbits a dIrr galaxy can be transformed into a dSph, conserving some signatures of this interaction. The final galaxy typically has a triaxial (mostly prolate) shape with some remnant rotation around the minor axis. A detailed discussion regarding the possible remaining effects of these interactions on the photometry of Fornax can be found in del Pino et al. (2015).

Kinematic measurements provide complementary information about the past of the galaxy. The fact that some rotation remains in Fornax may indicate a rotating progenitor for this galaxy. Figure 12 shows the Fornax perigalacticon passages expected from the orbital parameters estimated using the presently available proper motion measurements (for further information see del Pino et al. 2013, section 7.1). There is no clear correlation between perigalacticon passages and the dynamics of the galaxy, although our data do not cover stars distant enough to study possible tidal tails or other dynamical signatures from tidal stirring.

On the other hand, a drop in $|\mathbf{L}|$ can be noticed around the first perigalacticon passage, ~ 9.8 Gyr ago. This passage coincides with the change in the angular momentum orientation from the one pointing along $+b$ to the one pointing along $+a$. Interestingly, at the second passage (~ 6.2 Gyr

ago), when the rotation of the galaxy is around $-b$, we observe an enhancement of $|\mathbf{L}|$. Several scenarios could explain this effect, including the tidal stirring model. The orientation of the angular momentum of Fornax with respect to the MW potential during the perigalacticon passages could have influenced the orbits of the stars in Fornax. In fact, tidal effects are strongly dependent on the relative orientation of the angular momentum of the stars in the galaxy with respect to the orbital momentum of the galaxy around its host (see for example Lokas et al. 2015). Tidal forces are much more effective in weakening the rotation streaming motions for dwarf galaxies on prograde orbits. However, if a bar is present in the dwarf the host galaxy can also accelerate the orbits of the stars in the dwarf depending on the orientation of the bar at pericentre. For more details about how tidal forces can modify the pattern speed of the bar, we refer the reader to Section 6 of Lokas et al. (2014b).

Our results are qualitatively compatible with a scenario in which a disk progenitor of Fornax was on a prograde orbit around the MW at its first close fly-by, so that its angular momentum was reduced and its orientation changed. This first perigalacticon passage may have also resulted in the morphological transformation into a prolate (bar-like) spheroid. At the second perigalacticon, if the orientation of the bar with respect to the direction of the tidal force from the MW was favourable the angular momentum could have been increased again. Indeed this could be the case for stars born around 6 Gyr whose angular momentum is approximately orthogonal and prograde to the proper motion vector of the galaxy, $\theta_{\text{pm}} = 169^\circ \pm 8.5^\circ$ in the Fornax main axis system (Piatek et al. 2007). However, this scenario does not explain the sudden change of the orientation of the angular momentum ~ 8.7 Gyr ago, from the one along its positive minor main semi-axis ($+b$) to the one around its negative minor semi-axis ($-b$). Still, taking into account other possible tidal stirring signatures from photometry we can not rule out possible tidal interactions of Fornax with the MW in the past.

Another probable scenario of the evolution of Fornax could involve a merger between two or more stellar systems. This possibility have been considered in several works (Coleman et al. 2004; Yozin & Bekki 2012; Amorisco & Evans 2012). The basic idea relies on two disk galaxies colliding, each one with a particular angular momentum. As a result, the orbits of the stars are disturbed, showing more chaotic and random rotation patterns. After the merger the system would have a spheroidal shape and a relatively high velocity dispersion. This scenario is also compatible with more than one system being accreted and does not rule out the possibility of different kinds of galaxies colliding (e.g. a disk and a spheroid).

Some signatures could remain in the galaxy after these events for several Gyr: strange rotation patterns, shell-like structures, clumps or streams of stars, etc. Fornax appears to show some of these characteristics, making it very plausible that a merger had played an important role in its evolution or even formation. These features have already been discussed from the point of view of photometry in del Pino et al. (2013, 2015). In the present work, we revisit the problem using the information provided by spectroscopy, i.e. v_{LOS} and metallicity.

The existence of different rotation patterns as a func-

tion of the stellar age (see Figure 11) may point to an accretion of stellar material with different angular momentum at some time in the past. We have traced the preferred rotation direction as a function of the stellar age and found that approximately between 10 and 7.5 Gyr ago the rotating motion undergoes some fluctuations (see Figure 12). These changes may not be significant, since stars between 10 and 7.5 Gyr old show little streaming motion, i.e. low $|\mathbf{L}|$. After that, the galaxy appears to steadily recover the preferred rotating direction around its minor axis. Several scenarios could explain this behaviour, but probably the simplest and most straightforward is, indeed, a gas-rich merger between two dwarfs. We therefore find further support for the scenario proposed in del Pino et al. (2013, 2015): a major merger suffered by Fornax at $z \sim 1$. The violent event would have expelled a significant amount of gas which would then be accreted on to the deeper potential well of the resulting galaxy. This scenario would explain the conspicuous dynamical features shown by Fornax.

First, the gas from both progenitors could have had different angular momentum, resulting in a weaker angular momentum of the mixed gas. This effect has been also observed during major mergers in the Illustris simulation (Genel et al. 2015). The \mathbf{L} shows significant fluctuations starting at ~ 10 Gyr ago, with the largest change in its direction at ~ 8 Gyr ago. This would indicate some prolonged gravitational interaction between the progenitors until they finally merged. The latter is consistent with the scenario proposed by Amorisco & Evans (2012) in which Fornax is the result of a merger of a bound pair of galaxies. These galaxies would have interacted gravitationally, showing as a result the fluctuations observed in \mathbf{L} . This event would have also affected the SFH of the galaxy. In the top panel of Figure 12 we show the SFH for the three observed fields defined in del Pino et al. (2013): IC1, IC2 and OC. Some interesting correlations between the SFHs and the rotation direction can be observed. The first one shows itself at about 10 Gyr ago, when we see a strong burst of star formation in the outskirts of the galaxy. This was followed by the most intense burst of star formation, located in the central regions of the galaxy (IC1) at ~ 8 Gyr ago.

Second, the galaxy could have experienced an inflow of the previously expelled gas. Since this gas would not have had the same angular momentum as the galaxy, its accretion may have caused the chaotic rotation patterns observed in the younger populations. This gas would also be responsible of the shell-like structure found by Coleman et al. (2004).

This scenario would be consistent with comprehensive cosmological Λ CDM simulations of Local Group-like environments in which only very few mergers between dwarf galaxies happen later than $z \sim 1$ (Klimontowski et al. 2010). It is also consistent with the bound pair merger scenario proposed by Amorisco & Evans (2012) and with the chemical pre-enrichment of the inner shell structure (Olszewski et al. 2006).

7 CONCLUSIONS

We have detected rotating streams of stars in Fornax. This indicates that Fornax is a rather complex system with various rotating components and that its spheroidal shape is

the superposition of stellar components with distinct kinematics. BEACON has proved to be a useful tool for detecting these kinematic components.

Fornax rotates mainly around its minor optical axis with an average velocity of $\sim 12 \text{ km s}^{-1}$. This is consistent with Fornax being a triaxial system partially supported by rotation. However, its detailed chemo-kinematics is complex, showing multiple rotation patterns depending on the metallicity of the stars. Stars with metallicities $[\text{Fe}/\text{H}] \sim -1.1$ have more chaotic patterns, resulting in nearly complete lack of global rotation. On the other hand, more metal rich stars show strong rotation signal, but in the opposite direction with respect to the dominant rotation.

We have derived the age for the groups of stars using their metallicity distributions. Our results show that stars with ages around 8 Gyr ($z \sim 1$) change the direction of their rotation. We conclude that this change, together with the strong spatial gradients observed in the SFH as a function of radius (del Pino et al. 2013), and the more chaotic angular momenta shown by the younger populations are closely related. We propose a merger occurring at $z \sim 1$ as a plausible scenario for explaining all these features. This scenario is consistent with the results from photometry presented in del Pino et al. (2015).

We have also investigated the possible effects of tidal interactions of Fornax with the MW. Our results suggest that some interactions between Fornax and the MW could have occurred during the perigalacticons. The first one, that probably occurred ~ 9.8 Gyr ago coincides with an almost complete loss of rotation in the galaxy until ~ 7.5 Gyr ago. Moreover, the enhancement observed in the rotation signal during the second passage could also be caused by tides if the orientation of the stellar component was favourable. On the other hand, according to models by Mayer (2010), Fornax should have had its first perigalacticon passage after $z = 1$ in order to have such an extended star formation history. This, together with the lack of data at large enough distances from the galaxy, does not allow us to detect direct signatures of such interactions, e.g. tidal tails. Therefore, the relevance of these interactions for the evolution of Fornax remains unclear.

ACKNOWLEDGMENTS

The authors thank the referee, Dr. Mario Mateo for his thorough review and comments. We are grateful to Dr. G. Battaglia and Dr. E. Kirby for generously providing their data for this project, and to Dr. M. Monelli and Dr. S. Fouquet for their comments and suggestions which have helped to improve the manuscript. AdP also thanks S. Bertran de Lis for her support during this project. This research was partially supported by the IAC (grant 310394) and the Education and Science Ministry of Spain (grants AYA2010-16717, and AYA2013-42781-P). Further support has been provided by the Polish National Science Centre under grant 2013/10/A/ST9/00023.

REFERENCES

Amorisco N. C., Evans N. W., 2012, *ApJ*, 756, L2

- Ankerst M., Breunig M.M., Kriegel H., Sander J. 1999, in Proc. ACM SIGMOD Int. Conf. on Management of Data. ACM Press, New York, p. 49
- Battaglia G. et al., 2006, *A&A*, 459, 423
- Battaglia G., Helmi A., Tolstoy E., Irwin M., Hill V., Jablonka P., 2008, *ApJ*, 681, L13
- Battaglia G., Irwin M., Tolstoy E., Hill V., Helmi A., Letarte B., Jablonka P., 2008, *MNRAS*, 383, 183
- Battaglia G., Tolstoy E., Helmi A., Irwin M., Parisi P., Hill V., Jablonka P., 2011, *MNRAS*, 411, 1013
- Bate N. F., McMonigal B., Lewis G. F., Irwin M. J., Gonzalez-Solares E., Shanks T., Metcalfe N., 2015, *MNRAS*, 453, 690
- Binney J., 1985, *MNRAS*, 212, 767
- Bouchard A., Carignan C., Staveley-Smith L., 2006, *AJ*, 131, 2913
- Carrera R., Gallart C., Hardy E., Aparicio A., Zinn R., 2008a, *AJ*, 135, 836
- Carrera R., Gallart C., Aparicio A., Costa E., Méndez R. A., Noël N. E. D., 2008b, *AJ*, 136, 1039
- Coleman M., Da Costa G. S., Bland-Hawthorn J., Martínez-Delgado D., Freeman K. C., Malin D., 2004, *AJ*, 127, 832
- Coleman M. G., Da Costa G. S., 2005, *PASA*, 22, 162
- Coleman M. G., de Jong J. T. A., 2008, *ApJ*, 685, 933
- de Boer T. J. L. et al., 2012, *A&A* 544, A73
- de Boer T. J. L., Tolstoy E., Saha A., Olszewski E. W., 2013, *A&A*, 551, A103
- del Pino A., Hidalgo S. L., Aparicio A., Gallart C., Carrera R., Monelli M., Buonanno R., Marconi G., 2013, *MNRAS*, 433, 1505
- del Pino A., Aparicio A., Hidalgo S. L., 2015, *MNRAS*, 454, 3996
- Ebrová I., Lokas E. L., 2015, *ApJ*, 813, 10
- Fraternali F., Tolstoy E., Irwin M. J., Cole A. A., 2009, *A&A*, 499, 121
- Genel S., Fall S. M., Hernquist L., Vogelsberger M., Snyder G. F., Rodriguez-Gomez V., Sijacki D., Springel V., 2015, *ApJ*, 804, L40
- Greco C. et al., 2007, *ApJ*, 670, 332
- Greco C. et al., 2009, *ApJ*, 701, 1323
- Hendricks B., Koch A., Walker M., Johnson C. I., Peñarrubia J., Gilmore G., 2014, *A&A*, 572, A82
- Irwin M., Hatzidimitriou D., 1995, *MNRAS*, 277, 1354
- Kazantzidis S., Lokas E. L., Callegari S., Mayer L., Moustakas L. A., 2011, *ApJ*, 726, 98
- Kirby E. N. et al., 2010, *ApJS*, 191, 352
- Klimentowski J., Lokas E. L., Kazantzidis S., Mayer L., Mamon G. A., 2009, *MNRAS*, 397, 2015
- Klimentowski J., Lokas E. L., Knebe A., Gottlöber S., Martinez-Vaquero L. A., Yepes G., Hoffman Y., 2010, *MNRAS*, 402, 1899
- Koch A., Wilkinson M. I., Kleyna J. T., Gilmore G. F., Grebel E. K., Mackey A. D., Evans N. W., Wyse R. F. G., 2007, *ApJ*, 657, 241
- Koch A., Kleyna J. T., Wilkinson M. I., Grebel E. K., Gilmore G. F., Evans N. W., Wyse R. F. G., Harbeck D. R., 2007, *AJ*, 134, 566
- Letarte B. et al., 2010, *A&A*, 523, A17
- Lewis G. F., Ibata R. A., Chapman S. C., McConnachie A., Irwin M. J., Tolstoy E., Tanvir N. R., 2007, *MNRAS*, 375, 1364
- Lokas E. L., 2009, *MNRAS*, 394, L102
- Lokas E. L., Kazantzidis S., Mayer L., 2011, *ApJ*, 739, 46
- Lokas E. L., Majewski S. R., Kazantzidis S., Mayer L., Carlin J. L., Nidever D. L., Moustakas L. A., 2012, *ApJ*, 751, 61
- Lokas E. L., Athanassoula E., Debattista V. P., Valluri M., del Pino A., Semczuk M., Gajda G., Kowalczyk K., 2014a, *MNRAS*, 445, 1339
- Lokas E. L., Ebrová I., del Pino A., Semczuk M., 2014b, *MNRAS*, 445, L6
- Lokas E. L., Semczuk M., Gajda G., D'Onghia E., 2015, *ApJ*, 810, 100
- Mackey A. D., Gilmore G. F., 2003, *MNRAS*, 345, 747
- Mateo M., Olszewski E., Welch D. L., Fischer P., Kunkel W., 1991, *AJ*, 102, 914
- Mateo M. L., 1998, *ARA&A*, 36, 435
- Mayer L., Governato F., Colpi M., Moore B., Quinn T., Wadsley J., Stadel J., Lake G., 2001, *ApJ*, 559, 754
- Mayer L., 2010, *Advances in Astronomy*, 2010, article id. 278434
- McConnachie A. W., 2012, *AJ*, 144, 4
- Muñoz R. R. et al., 2005, *ApJ*, 631, L137
- Olszewski E. W., Mateo M., Harris J., Walker M. G., Coleman M. G., Da Costa G. S., 2006, *AJ*, 131, 912
- Piatek S., Pryor C., Bristow P., Olszewski E. W., Harris H. C., Mateo M., Minniti D., Tinney C. G., 2007, *AJ*, 133, 818
- Piatti A. E., del Pino A., Aparicio A., Hidalgo S. L., 2014, *MNRAS*, 443, 1748
- Pont F., Zinn R., Gallart C., Hardy E., Winnick R., 2004, *AJ*, 127, 840
- Poretti E. et al., 2008, *ApJ*, 685, 947
- Starkenbourg E. et al., 2010, *A&A* 513, A34
- Strigari L. E., Frenk C. S., White S. D. M., 2010, *MNRAS*, 408, 2364
- Tammann G. A., Sandage A., Reindl B., 2008, *ApJ*, 679, 52
- van den Bergh S., 1999, *A&ARv*, 9, 273
- Walker M. G., Mateo M., Olszewski E. W., Bernstein R., Wang X., Woodroffe M., 2006, *AJ*, 131, 2114
- Walker, M. G., Mateo, M., Olszewski, E. W. 2008, *ApJ*, 688, L75
- Walker M. G., Mateo M., Olszewski E. W., 2009, *AJ*, 137, 3100
- Walker, M. G., Mateo, M., Olszewski, E. W., Peñarrubia, J., Wyn E. N.; Gilmore, G. 2009, *ApJ*, 704, 1274
- Walker, M. G., & Peñarrubia, J. 2011, *ApJ*, 742, 20
- Weijmans A.-M. et al. 2014, *MNRAS*, 444, 3340
- Wheeler C., Pace A. B., Bullock J. S., Boylan-Kolchin M., Onorbe J., Fitts A., Hopkins P. F., Keres D., 2015, arXiv:1511.01095
- Wilkinson M. I., Kleyna J. T., Evans N. W., Gilmore G. F., Irwin M. J., Grebel E. K., 2004, *ApJ*, 611, L21
- Wolf J., Martinez G. D., Bullock J. S., Kaplinghat M., Geha M., Muñoz R. R., Simon J. D., Avedo F. F. 2010, *MNRAS*, 406, 1220
- Yozin C., Bekki K., 2012, *ApJ*, 756, L18